Light-Enhancing Plasmonic-Nanopore Biosensor for Superior Single-Molecule Detection

*Ossama N. Assad, Tal Gilboa, Joshua Spitzberg, Matyas Juhasz, Elmar Weinhold, and Amit Meller**

The development of nanopore-based biosensors has received considerable attention in the past two decades due to their compatibility with a broad range of analytes, including nucleic acids,[1] proteins,[2] and various small molecules.[3] Particularly, nanopore-based DNA sequencing has recently emerged as a viable alternative to sequencing-by-synthesis approaches,[4] offering a highly portable and affordable solution with high throughput and precision.[5,6] Currently the most advanced nanopore-based sequencing methods are based on protein pores, such as the CsgG or MspA channels, which require a ratcheting enzyme to regulate the transport of a DNA strand.[6] Nevertheless, the development of synthetic nanopores remains a major focus in nanotechnology due to the inherent limitations of the protein pores and the greater flexibility that synthetic nanopores offer in term of the ability to tailor their size, shape, and surface properties toward specific sensing applications.[4,7]

Solid-state nanopores (ssNPs) fabricated in thin inorganic membranes can be crafted with sub-nanometer precision to match the size of the target analyte, and are therefore considered to be highly attractive platforms. Moreover, ssNPs are compatible with a variety of single-molecule detection methods (in addition to the ion-current resistive-pulse technique) making them ideally suited for the development of future integrated biological sensors.[8,9] In particular, because ssNPs are fabricated in essentially 2D, solid membranes, they lend themselves to relatively straightforward implementation of optical sensing, which can provide independent and completely orthogonal information on the analytes. As a result, in the past few years electro-optical sensing in ssNPs has gained growing momentum toward applications such as rapid DNA sequencing, DNA barcoding, and epigenetic modification sensing.[9–12] Notably, ssNPs can be articulated with plasmonic nanostructures to enhance key features of the nanopore sensing. For example, plasmonic structures have been used to produce local heating in the pore vicinity, hence controlling the translocation speed and capture rate of DNA molecules.[13,14] Moreover, bow-tie structures fabricated around the nanopore were proposed for rapid DNA sequencing utilizing surface-enhanced Raman scattering from nucleotides passing through the pore.[14,15]

Despite these major advancements in optical sensing in ssNPs, the detection of individual fluorophores has proven to be challenging due to two competing factors: first, when excited by the laser source, solid dielectric membranes (such as SiN_x, SiO_2, etc.) emit light through photoluminescence in wavelengths that overlap with the fluorescence emission.[11,12] This background noise comes on top of the fluorescence background from molecules residing in the detection volume. Second, the dwell time of the fluorophore in the nanopore is relatively short, hence limiting the photon integration time and diminishing the overall signal. A possible solution for these issues involved the incorporation of molecular quenchers for each fluorophore,[9,11] but this comes at the expense of more complex sample preparation. In this study we present a radically improved and more general approach, which produces much stronger signal and orders of magnitude smaller background in a quencher-free system. This is achieved by embedding the nanopore in a subwavelength plasmonic nanowell (PNW), serving three main functions: First, the thin metal coating of the SiN_x membrane essentially blocks the incident light from exciting the molecules at the *cis* side (entry side) of the membrane, in the same principle employed in zero-mode waveguide (ZMW) devices used for single-molecule optical DNA sequencing by synthesis.[16,17] This practically eliminates the fluorescence background even when the concentration of the analyte in *cis* is extremely large—a highly desired feature for high-throughput sensing. Second, unlike the ZMWs in which the metal layer faces the labeled analytes, in our case the SiN_x membrane is facing the analyte source allowing the nanopore to act as a physical gate, hence sending individual DNA molecules into and through the optical sensing volume one at a time, and exposing them to light only after their passage through the aperture. This molecular gating is monitored in real time by detecting the ion current flow through the pore providing crucial temporal synchronization used to further eliminate false optical bursts. Third, our design produces marked fluorescence amplification due to local enhancement of the electric field intensity inside the metallic PNW cavity coupled with quantum efficiency enhancement of the fluorophores. We illustrate this by probing covalently labeled double-stranded DNA molecules, threaded inside an ssNP drilled in the PNW cavity. Finite-difference time-domain (FDTD) simulations of the electromagnetic (EM) field in our device model yield comparable amplification ratio, further supporting our

Dr. O. N. Assad, T. Gilboa, J. Spitzberg, Prof. A. Meller
Department of Biomedical Engineering
The Technion –Israel Institute of Technology
Haifa 32000, Israel
E-mail: ameller@technion.ac.il
Dr. O. N. Assad, Prof. A. Meller
Department of Biomedical Engineering
Boston University
Boston, MA 02215, USA
M. Juhasz, Prof. E. Weinhold
Institute of Organic Chemistry
RWTH Aachen University
Landoltweg 1, Aachen 52056, Germany

DOI: 10.1002/adma.201605442

experimental results, and are in agreement with previous studies.[18,19]

To create the PNW–NP devices, we developed a wafer-scale nanofabrication method for manufacturing arrays of subwavelength plasmonic wells in a thin opaque layer of gold deposited on freestanding low-stress silicon nitride membranes.[17,20] The fabrication process consists of three main steps, described in details in Figure S1 in the Supporting Information. Briefly, in the first step, a high-resolution negative tone patterning was used to define nanopillars of the photoresist on the wafer surface, followed by evaporation of 130 nm gold film onto the substrate. The pillars were then dissolved along with the metal on them using lift-off techniques, leading to the formation of nanometric wells in the gold film. In the second step, a hard mask consisting of windows and dice lines was opened on the reverse side of the wafer using reactive ion etching, followed by anisotropic wet etch of silicon to create a freestanding SiN_x membranes, which overlap with the metallic nanowell arrays. Finally, high-resolution transmission electron microscopy (TEM) was used to fabricate nanopores in the center of the nanowells. Except where stated, the membranes consisted of 25 nm thick freestanding windows of SiN_x ≈30 µm × 30 µm in size. These membranes were subsequently thinned down using controlled buffered oxide etch process, leading to sub 10 nm thick regions in the well base where pores were drilled. This wafer-scale fabrication method results in arrays of precisely controlled and spaced nanowells.

Figure 1a displays schematically the PNW–NP device. In this illustration, the front side of the SiN_x membrane (light green) and the Au layer (orange) are facing down. We conventionally define the *cis* and *trans* chambers as the analyte's source and drain compartments, respectively. For negatively charged molecules such as DNA, the *trans* chamber is positively biased to drive translocation from *cis* to *trans*. The fabricated devices were thoroughly characterized using a combination of methods. In the first stage, optical microscopy was used as a high-throughput method to measure variability either within the nanowell arrays or between fabricated devices. Figure 1b shows an optical bright-field image of 7 × 6 arrays of nanowells with 5 µm interspacing supported by ≈30 µm × 30 µm of freestanding SiN_x membrane. The arrays appear to be properly aligned and devoid of any structural defects. In the second stage, scanning electron microscopy was used to characterize the fabricated nanowells. Figure 1c shows scanning electron microscopy (SEM) images of individual nanowell, taken from the Au side. The magnified image shows the presence of smooth side walls that enables a proper entrance of single molecules inside the nanowell. Finally, high-resolution transmission electron microscopy (TEM) measurements confirmed the physical dimensions and uniformity of the nanowells and the pores drilled in their center. Figure 1d,e shows TEM images of a typical nanowell with 120 nm in diameter that contains a ≈4 nm pore at different resolutions.

To characterize the optical properties of the PNW–NP device and its ability to suppress background, we measured the fluorescence emission from suspensions of freely diffusing dyes (Cy5) in large range of concentrations, from 10^{-12} M to 10^{-9} M, relevant for single molecule analyses. The measurements were

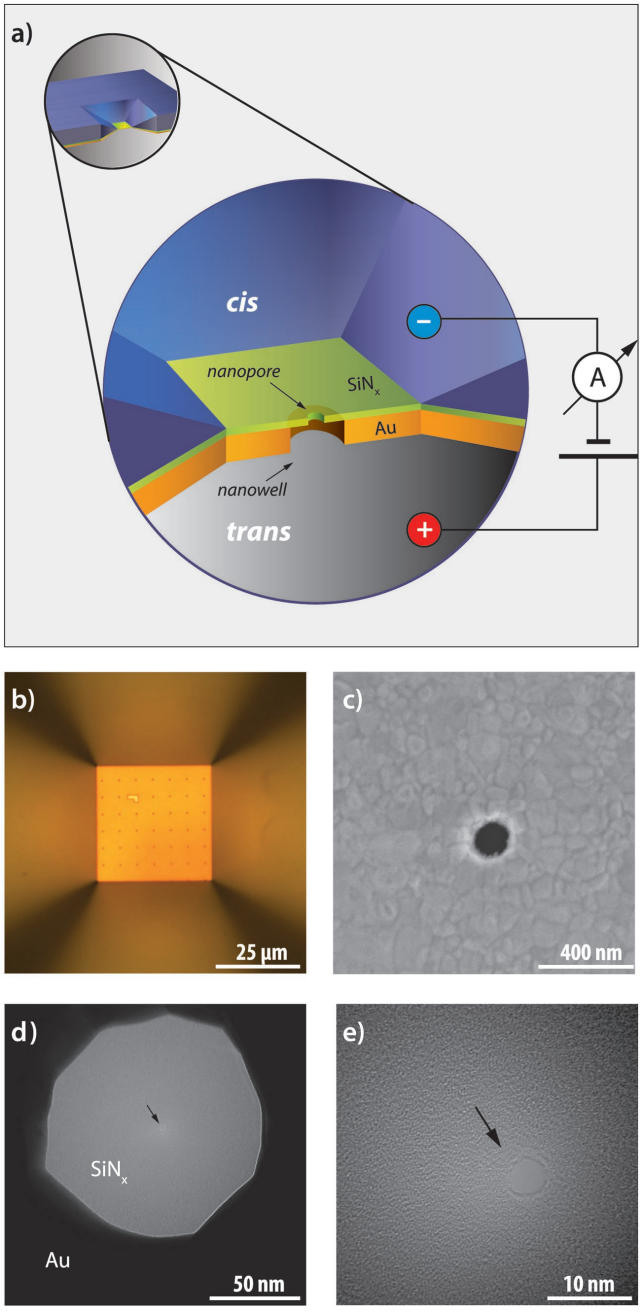

Figure 1. A plasmonic nanowell–nanopore (PNW–NP) device architecture for enhanced single molecule fluorescence detection. a) Schematic cross-section of the PNW-NP device containing a nanowell fabricated in a gold film (orange) with a nanopore drilled in the freestanding SiN_x membrane (light green). b) Bright-field optical microscopy image (back view) of a nanowell array with 5 µm pitch fabricated on ≈30 µm × 30 µm freestanding SiN_x membrane. An "L" shape orientation marker (bright pattern on image) is fabricated on each device to facilitate nanowell identification. c) Scanning electron microscopy (SEM) image (top view) of a typical nanowell with diameter of 120 nm, fabricated in a 130 nm thick polycrystalline Au films. d) Transmission electron microscopy (TEM) image (top view) of a single nanowell with a nanopore drilled in its base. The bright spots in the center (arrow) correspond to the nanopore. e) High-resolution TEM image shows a close up view of the drilled ≈4 nm pore.

performed using a custom confocal microscope (see the Supporting Information) equipped with an avalanche photodiode (APD) detector for single molecule sensing. We examined two different configurations of the device: first a "ZMW" configuration, in which the excitation laser is introduced from the SiN_x membrane side and the dyes are inserted at the nanowell side. Second, a "PNW" configuration, in which the laser excitation is introduced from the Au (nanowell) side and the dyes are inserted at the SiN_x membrane side. In all cases, the emission light is collected in epifluorescence mode (same side as the excitation). Additionally, we measured a standard nanochip device ("STD") lacking the Au nanowell. In each measurement the confocal excitation and emission spots were carefully aligned to perfectly overlap with the SiN_x membrane in the z direction, and centered in the lateral axes over the nanowell using a nanopositioner, by recording the elastic and nonelastic backscattering, as shown in the Supporting Information. As a reference we also measured the background signal from pure ddH_2O sample (filtered using a 0.02 µm syringe filter) for each device configuration.

In **Figure 2**a, we show representative 20 s time traces of the fluorescence intensities measured using either the ZMW configuration (red lines) or the PNW configuration (green lines) for three different Cy5 concentrations (1×10^{-12}, 1×10^{-9}, and 100×10^{-9} M). Additional data sets are provided in the Supporting Information. At the lowest concentration (1×10^{-12} M) both configurations show flat traces with an average value equal to the reference level. At 1×10^{-9} M we can observe single-molecule bursts in the ZMW trace, but not in the PNW configuration. These bursts represent single molecules entering sporadically the nanowell volume. At 100×10^{-9} M we observe an increase in the baseline level of the ZMW configuration, but the PNW configuration level remains flat at the reference level. These results indicate that even at high dye concentration background emission light does not "leak" through the Au layer or the nanowell. Importantly, the apparent background level of the PNW configuration remains at the water reference level regardless of dye concentration, hence providing nearly ideal baseline for single molecule detection.

To characterize the net fluorescence background in each of the configurations, we measured the average emission intensity for each Cy5 dye concentration and normalized it by the reference to obtain the net fold increase relative to ultrapure water. Our results are summarized in Figure 2b, where we show the average emission as a function of Cy5 concentration from 1×10^{-12} to 1×10^{-6} M. Focusing first on the STD device (blue markers), we observe at extremely small dye concentration an averaged baseline background level of 1, as expected, but above roughly 0.1×10^{-9} M we observe a linear increase of the intensity with Cy5 bulk concentration (solid line). We note that above this concentration single fluorophore detection is practically unfeasible due to the presence of more than a single molecule in the confocal volume (roughly 0.05 fL). The ZMW configuration (red symbols) greatly improves this situation as the Au layer blocks the excitation in the top chamber, and hence it effectively reduces the observation volume to a fraction of the nanowell volume (i.e., <1.5 aL), allowing single molecule measurements to take place up to $\approx 100 \times 10^{-9}$ M. Finally, the PNW configuration (green symbols) does not appear to be affected by the Cy5 concentration and remain at the baseline level through the entire concentration range tested.

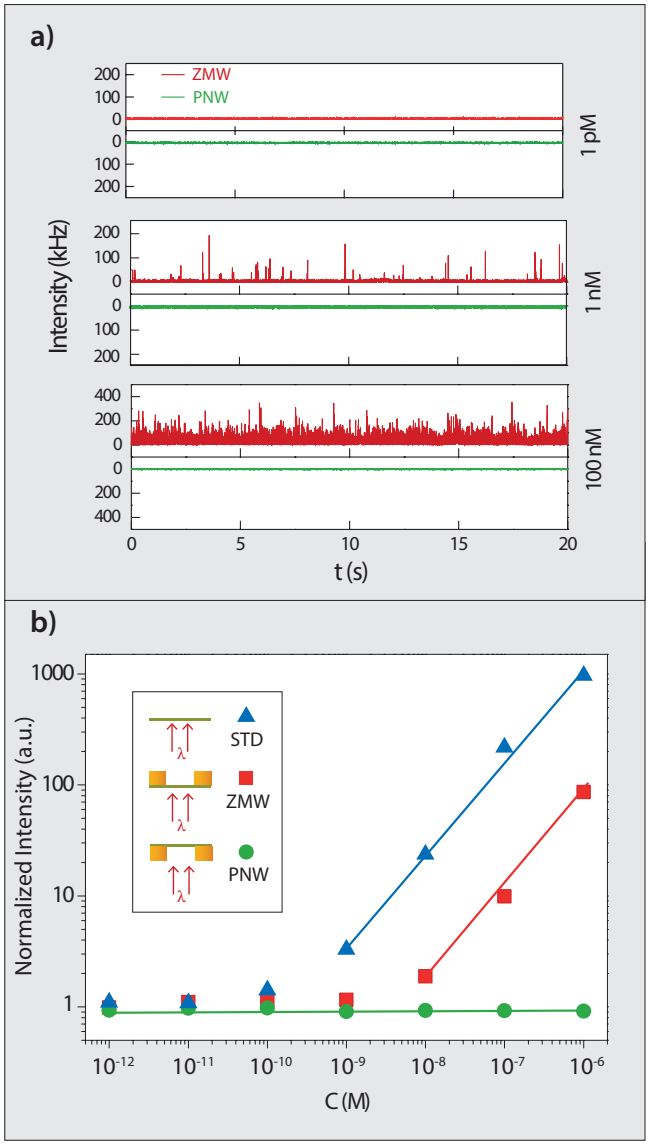

Figure 2. Fluorescence intensity measurements for free fluorescence dye (Cy5) obtained under red laser excitation (640 nm, 90 µW). a) Representative fluorescence intensity time traces (raw counts) comparing the ZMW (red) and PNW (green) device configurations. The three panels correspond to three different dye concentrations: 1×10^{-12} M upper panel, 1×10^{-9} M middle panel, and 100×10^{-9} M lower panel (see the Supporting Information for full data sets). b) Normalized photon count rate as a function of dye concentration for three device configurations (inset: schematic of the excitation modes): 1) STD, standard nanochip device, in which the excitation laser form a diffraction-limited focal spot on the SiNx membrane and the dyes are inserted from the opposite side of the membrane (blue triangles), 2) ZMW, in which the excitation laser is introduced from the SiN_x membrane side and the dyes are inserted at the Au (nanowell) side (red squares), and 3) PNW, in which the laser excitation is introduced from the Au (nanowell) side and the dyes are inserted at the SiN_x membrane side (green circles). Data are normalized to the background fluorescence (water solution only) of each device configuration to permit comparison. Lines are guides to the eye.

Taking advantage of the extremely low optical background level obtained in the PNW configuration, we hypothesized that it would be possible to electrophoretically draw and detect individual labeled molecules through the nanowell. Presumably this can be achieved by drilling a nanopore at the bottom SiN_x membrane of the nanowell that acts as a "gate," hence sending individual analytes into the nanowell. Moreover, by measuring the ion current flowing through the nanopore, precise electrical time gating signals can be obtained for the translocation of each molecule. Since the nanopore can only accommodate one analyte molecule at a time, it circumvents crowding of multiple molecules in the nanowell sensing volume.

To check this hypothesis, we constructed an electro-optical sensing apparatus for the simultaneous detection of the ion current flowing through the nanopore ($I_E(t)$) and the optical photon flux ($I_O(t)$) emitted in our device. Our system involves a custom made stage-scanning confocal microscope with a high numerical aperture water immersion objective (N.A. = 1.25), described schematically in **Figure 3**a. Briefly, the PNW–NP devices are mounted in a special fluidic cell, which on one hand form two electrically separated fluid chambers ("*cis*" and "*trans*" chambers), and on the other hand is equipped with a bottom quartz cover slide for low-background single-molecule epifluorescence excitation/emission. The cell is placed in a nanopositioner stage for precise alignment of the device with the tightly focused laser spot and the optically conjugated confocal volume. To ensure perfect alignment, our system also includes a photodiode, located at a conjugated plane to the focal spot for the detection of the backscattered light. Alignment is obtained when both the backscattered light and the photoluminescence (originated from the SiN_x membrane) reach their corresponding minima/maxima in the *x*, *y*, and *z* directions. The alignment procedure of the PNW–NP is described in details in Figure S4 in the Supporting Information.

To characterize the electro-optical properties of PNW–NP, we labeled a 5 kbp double stranded DNA molecules with the high-brightness fluorophore CF640R (Biotium, USA, ex./em. 642/662 nm), as explained in the Supporting Information. Each DNA molecule harbors 7 fluorophores covalently conjugated to an adenine residue at the specific sequences (5′-TCGA-3′) using methyltransferase reaction.[21] The labeled DNA molecules were introduced to the *cis* chamber at relatively low concentration (10×10^{-12} M or less) for electro-optical translocation measurements. The device is first aligned with the laser to obtain stable open-pore current, after which DNA is introduced. Typical concatenated sets of events collected using either the STD device (no nanowell) or the PNW–NP device are shown at the top panels of Figure 3b,c, respectively. In each case the electrical and optical signals (blue and red lines, respectively) were measured simultaneously. The laser power (set to 90 µW at the back aperture of objective) and other experimental conditions were unchanged. Looking at Figure 3b,c, we note three salient differences: First and foremost, we observe a nearly tenfold increase in the peak intensities of the events acquired with the PNW–NP device as compared with the STD device. This apparent enhancement in the detected fluorescence intensity is further analyzed in Figure 5. Second, in the STD device about 16% of all optical events ($N = 493$) lack a corresponding electrical resistive pulse (an electrical event), as marked with black asterisks in Figure 3b. In contrast, all the optical events in the PNW–NP device ($N = 272$) are accompanied by an electrical resistive pulse. Third, a closer analysis of the time delay between the rise of the optical and electrical events reveals that in the case of the STD device, most of the optical signals begin prior to their corresponding electrical events, but in the PNW–NP device this situation of the signals appears to be nearly synchronized. This pattern is exemplified in the zoom-in views of two representative events shown in Figure 3b,c bottom panels.

To perform a statistical analyses of all the data, we developed an offline software to identify simultaneous electrical/optical events, as follows: first a smoothed version of $I_E(t)$ was used to identify the start time, end time, and dwell time of each of the electrical blockade events by applying a threshold to the data at three standard deviations away from the open pore level. These time tags were used to extract the corresponding data points in the optical signal $I_O(t)$, along 24 ms of paddings before and after each event. $I_O(t)$ was also subjected to smoothing and thresholding to find the beginning and ending the corresponding optical event, as shown in **Figure 4**a. In Figure 4b, we compare the translocation dwell time distributions measured using a STD device (blue markers) and PNW–NP device (gold markers). The nanopores in these devices were nearly the same size (≈4 nm, open pore current 5.0 ± 0.1 nA). The two measurements yielded nearly the same characteristic dwell times (320 ± 15 and 358 ± 18 µs for the STD and PNW–NP, respectively) obtained by tail fit of the distributions by exponential functions. This small difference (about 10%) in the characteristic time can be attributed to slight difference in the nanopore size itself, demonstrating the PNW has little effect on the dwell-time of the DNA in the nanopore.

We next extracted the time delay between the rise of the optical signal and the resistive ion current blockade (δt_{O-E}) for each and every event in our datasets. Starting from the STD device we notice that the optical photon current in the majority of the events (≈95%) rise prior to the onset in the electrical blockade event (light blue bars), and even more importantly that the distribution of these times is extremely broad. For example, some DNA molecules arrive in the close vicinity of the pore 20 ms before physically entering the pore. This observation is in line with previously published models describing the capture process of DNA onto nanopores: following a rapid drift of the negatively charged DNA toward the pore, one of its ends must be threaded before translocation is commenced.[22,23] These processes give rise to timescales that can be significantly longer than the translocation time itself. The roughly 5% minority events in which our algorithm identified the onset of the optical event past the electrical one, can be attributed to misidentification due to noise in the optical signal measured in the STD device. In contrast, the PNW–NP device (gold color) produced a nearly uniform delay time histogram, in which the optical signal in over 95% of the events started synchronously with the electrical signals or at a short delay after the electrical begin time. Specifically, the characteristic variation in δt_{O-E} measured in the PNW–NP device is on par with its electrical translocation dwell time distribution (≈360 µs). This data shows that Au PNW structure stacked on top of the nanopore ensures that the optical and electrical signals start times are practically synchronized with respect to each other, removing

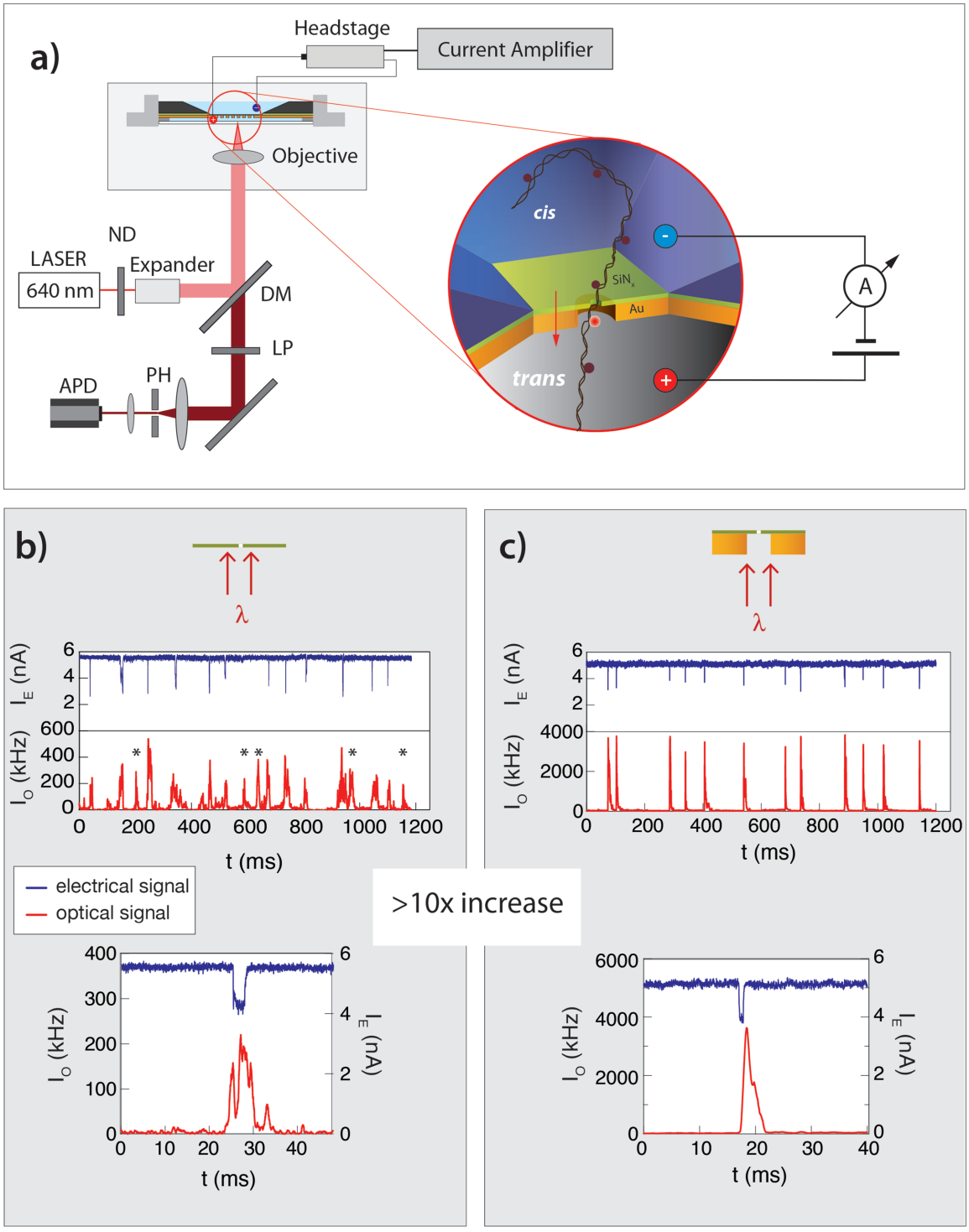

Figure 3. Simultaneous electrical and optical recording of DNA translocations through solid-state nanopores. Upper left panel: simplified illustration of the electro-optical nanopore setup. A collimated laser beam (640 nm) is focused at the nanopore region through the microscope objective lens, forming a tight focus spot for confocal illumination. The emitted photons are directed to an avalanche photo diode. Upper right panel: schematic illustration of the DNA translocation process, in which the ionic current flowing through the nanopore and the fluorescence emissions are probed in a synchronous manner. Entries and transport of labeled DNA molecules are recorded as transitions in the ion current and photon burst. Lower panels: representative electro-optical traces of DNA translocation events recorded using two device configurations: b) "STD" and c) "PNW–NP." Each panel presents concatenated typical traces of 5 kbp DNA covalently labeled with seven CF640R dyes, and a close-up view of a representative single translocation event. Electrical ion current shown in blue and optical signals in red. Asterisks correspond to photon spikes that are not associated with DNA translocations, observed only in the STD device. The optical translocation signal recorded using the plasmonic nanowell-nanopore configuration is enhanced by a factor of 10 as compared to the standard nanochip device configuration.

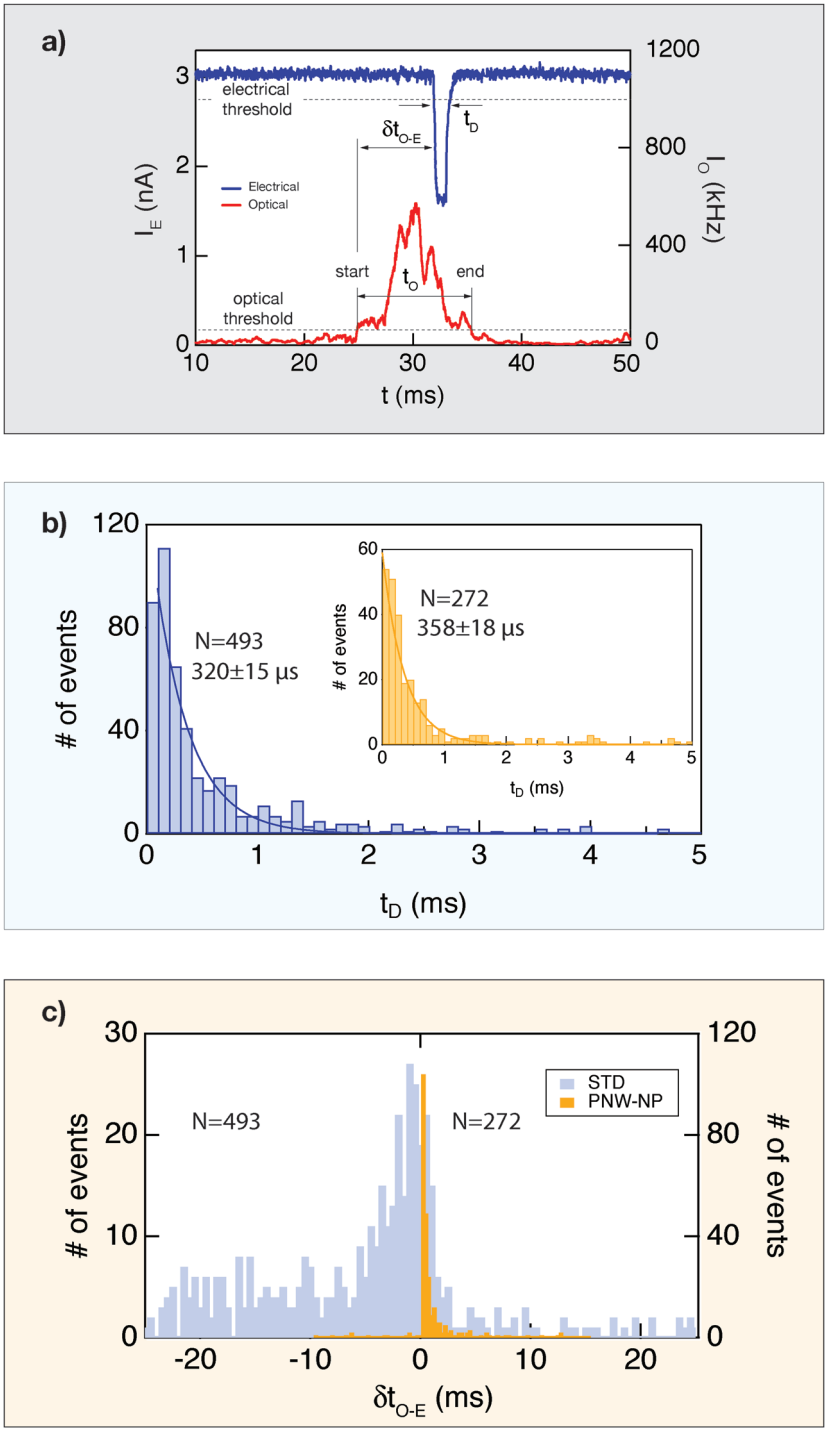

Figure 4. Analysis of the optical and electrical translocation dynamics. a) Zoom-in view of a typical DNA translocation event (STD device). Thresholds set at 3 standard deviations away from baseline levels for both the electrical and optical signals (dashed lines) were used to extract the electrical dwell time (t_D) the optical dwell time (t_O), start time (t_{start}), and end time (t_{end}) of the electrical and optical events. b) Distributions of t_D measured using STD device (light blue bars) and PNW–NP device (inset- gold bars). The data are fitted by exponential functions (solid lines). c) Distributions of the time delay between the rise of the optical and electrical signals (δt_{O-E}) measured using STD device (light blue bars) and PNW–NP device (gold bars). The number of events is indicated in each case. In the PNW–NP device the start time of the electrical and optical times are practically synchronized.

the heterogeneity in the optical start time measured in the STD device. Hence the nanopore acts as a gate, sending individual DNA molecules to the optical sensing zone one at a time, and providing an electrical gating signal. These measurements were reproduced at two different laser intensities (90 and 9 µW) giving similar results. Event diagrams showing the blockade current level versus electrical dwell time as well as the fluorescence intensity versus optical dwell time are shown in the Supporting Information.

Thus far we have shown that the PNW–NP structure provides two essential benefits for single-molecule electro-optical detection in solid-state nanopores, namely: an essentially fluorescence-free background even at high concentrations (Figure 2) and time synchronization between the electrical and optical signals (Figure 3 and 4). We next wished to quantify possible enhancements to the fluorescent signal itself in the PNW–NP biosensors. Fluorescence enhancement in cylindrical Au nanowell structures fabricated on glass substrates have been observed by several groups in the past.[18,19] Specifically, Gérard et al. employed fluorescence correlation spectroscopy to evaluate the count rate per fluorophore using the red fluorophore Alexa 647.[18] Their devices (cylindrical wells fabricated in 200 nm thick Au layer and diameter of 120 nm on glass substrate) bear similar geometry to our PNW design. Interestingly, two sources of enhancements were identified: i) local enhancement of the electromagnetic field intensity, particularly near the boundaries of the NW, and ii) enhancement of the fluorophore's quantum efficiency, presumably due to an increase in the density of electronic states of the fluorophore.

In order to confirm that our PNW devices are expected to boost fluorescence intensity with 640 nm excitation, and to evaluate the optimal PNW diameter, we performed detailed numerical simulations of our device. A model of our PNW–NP structure was constructed in a FDTD simulation, as described in the Supporting Information. Our results are summarized in top panels of **Figure 5**. We first compared the electromagnetic field intensity distribution in the reference STD device with the PNW–NP device. Both devices were aligned in 3D with respect to the nanopore location, and were excited by identical EM field from the Au side. The ratio of the resulting EM field intensities (PNW–NP over STD) are shown as 2D heat map in Figure 5a. Maximal enhancement

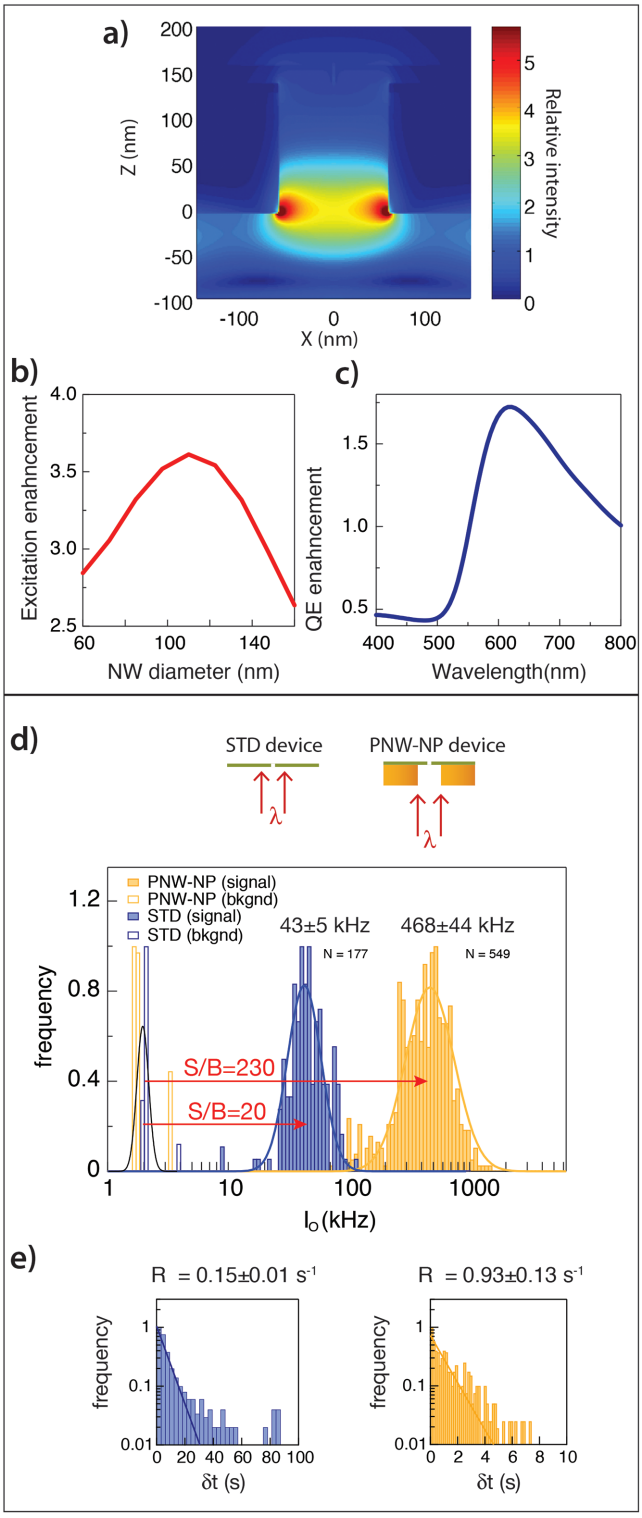

Figure 5. Fluorescence enhancement of single molecule translocation through a plasmonic nanowell-nanopore device. Top panels: results from FDTD simulations. a) 2D heat map of the excitation intensity calculated for a 120 nm PNW–NP device relative to the STD device illuminated from the Au side. b) The excitation enhancement factor as a function of the Au nanowell diameter at 640 nm. c) Spectrum of the quantum yield enhancement versus wavelength, calculated at the entrance of the nanowell. Bottom panels: Experimental fluorescence enhancement measurements using the PNW–NP (4 nm nanopore), compared to STD device. d) Semilog histograms of the net fluorescence intensity during 5 kbp DNA translocation measured using 9 μW laser power for the STD (blue) and PNW–NP (gold) devices. Histograms of the corresponding background levels are shown as empty bars. Data is fitted by Gaussian functions (solid lines). e) DNA translocation events rate for the STD and PNW–NP devices as in panel (d).

factor of nearly fourfold is observed at the center of the PNW aperture ($x = y = z = 0$). Notably, in addition to the increase in the field amplitude, the "focusing" of the electromagnetic field onto the PNW opening creates a desirable effect of constricting the excitation to a much smaller zone than the confocal spot (roughly 20 vs 200 nm).

In Figure 5b, we calculated the excitation enhancement at this spot for varying PNW diameter. In agreement with previous studies[18,19] the maximum enhancement for the red laser excitation occurs around a 120 nm diameter. Finally, we calculated the effect of the PNW on the quantum efficiency (QE) enhancement of the fluorophores (Figure 5c). Following the studies of Kinkhabwala and co-workers,[24] we approximated the enhancement in QE compared to pure water (similar to previous studies we assume that the intrinsic decay rate is unchanged by environment). Our results show a relative enhancement at the emission wavelength 660 nm of roughly 1.6. Thus, the expected overall fluorescence enhancement in our system can be estimated as the multiplication of both contributions, namely: $3.6 \times 1.6 = 5.8$.

Based on the previous studies of similar PNWs and our own FDTD simulations, we fabricated a 120 nm diameter PNW with a 4 nm NP drilled at its bottom surface, and performed electro-optical translocations experiments using 5 kbp DNA molecules labeled with seven CF640R fluorophores. As a reference we fabricated a STD device and performed similar electro-optical measurements keeping the same laser intensity of 9 μW and 300 mV bias. Our results are presented in Figure 5d using the same color codes as before (STD device in blue and PNW–NP in gold). The net photon intensity was evaluated in an event-by-event basis by first subtracting its background contribution measured prior to the beginning of the event. Events which did not show simultaneous electrical and optical rise/drop, respectively, were disqualified from this analysis. We then calculated the total net photons emitted during each event, as explained in Figure 3a, and normalized by its corresponding time (t_O) to obtain the average fluorescence intensity for each event. In this way, we avoided biasing of the distributions by a minority of the extremely long dwelling (and hence apparently very bright) events. The fluorescence intensity histograms presented as solid bars on a semilog scale were fitted by Gaussian functions having peaks at 43 ± 5 and 468 ± 44 kHz for the STD and PNW–NP devices, respectively. These values reflect photon emission rate of ≈6.1 and 69 kHz per fluorophore for the STD and PNW–NP devices, respectively. We also measured the fluorescence background level from each event by averaging roughly 24 ms of the data streams before the beginning of each optical event. The histograms of these values are shown as empty bars in Figure 5d. Both configurations resulted in similar background level (2.0 ± 0.1 kHz).

Based on the mean signal and background levels we can evaluate the S/B (signal/background) ratios for the two configurations, as shown in Figure 5d. We obtain S/B of 20 and 230 for the STD and PNW–NP devices, respectively, reflecting more than tenfold enhancement in the fluorescence signal. Recalling that these signals result from seven fluorophores we estimate that the S/B ratios per fluorophore are roughly 3 and 33 for the STD and PNW–NP devices, respectively. We note that an S/B of 33 for PNW–NP is significantly better than the quencher-based system.[9,11] As shown in Figure 5e, the event rate measured using the PNW–NP device is roughly sixfold larger than the corresponding one measured in the STD device. Since the experiments were performed using the same voltage (300 mV), DNA molecules and nanopore size (4 nm) primarily reflect the roughly sixfold larger DNA bulk concentration used.[23] Going back to Figure 2, we recall that the background level attained using the PNW–NP was practically independent of dye concentration, whereas the STD device was linearly increasing with concentration. Figure 5d therefore illustrates both gain in net signal and suppression of the fluorescence background in the plasmonic device. These results were further confirmed by repeating the measurements using stronger laser intensity (90 μW) as shown in the Supporting Information.

Plasmonic nanopore devices have recently been utilized by a number of groups primarily to produce local and highly switchable heating using near-infrared excitation.[13,25] Specifically, bow-tie plasmonic structures fabricated in the nanopore vicinity have been shown to enhance the nanopore functionality by increasing the event rate or gating its open state. Other researchers produced nanopores inside ZMW wells to enhance the capture of DNA capture required to prime the DNA sequencing by synthesis.[17] In this study we focused on the optical enhancing properties of plasmonic nanostructures coupled to a single-molecule nanopore sensor. Three main functions of the device were evaluated and studied: The ability of the device to suppress fluorescence background, enhance the fluorescence signal, and synchronize the optical and electrical signals. To this end we fabricated, experimentally characterized, and simulated PNW–NP devices designed to improve single-molecule light detection efficiency. Our gold nanowell design is inspired by previous studies, which observed fluorescence enhancement of Au nanowell fabricated on glass.[18,19] Importantly, the ability to fabricate nanowells on freely suspending thin SiN_x membrane enabled us to form a nanopore at the bottom of the nanowell, immerse the device from both sides in aqueous buffer, and translocate DNA through the PNW–NP hot-spot while characterizing its optical properties.

Our results highlight the advantageous aspects that the PNW–NP devices provide toward optical detection of single DNA molecules in nanopores. i) Fluorescence background is suppressed to effectively a constant level that essentially is independent of bulk dye concentration in the *cis* chamber. ii) Electrical-optical start time are synchronized, thereby nearly eliminating the stochastic variability associated with the DNA motion near the nanopore. This allows using the electrical ion current pulse as a gate signal to precisely indicate on the rise of the optical signal. iii) A tenfold net enhancement in the observed fluorescence intensity resulting at an extremely bright fluorescence (69 kHz per fluorophore) measured at very low laser excitation (9 μW). The light enhancement, background suppression, and high photon emission per fluorophore achieved at extremely small light intensity, open new opportunities for integration of ultralow power light emitting sources for future sophisticated but compact PNW–NP devices. Our results are supported by numerical simulations of the electromagnetic field intensity in the device and the QE enhancement of the fluorophore, which yield comparable enhancement factors.

The ability to suppress background, enhance the fluorescence, and synchronize the nanopore signals may open up new areas for nanopore-based sensing where combined electro-optical sensing can be utilized. Some applications include high sensitivity genotyping based on extremely small DNA copy numbers, DNA sequencing, and epigenetic markers quantification.

Supporting Information

Supporting Information is available from the Wiley Online Library or from the author.

Acknowledgements

The authors are grateful to C. Torfstein for her assistance in nanopore fabrication and sample characterization. Fabrication and characterization of the PNW–NP devices are performed at Harvard University CNS and at the Technion MNF & PU facilities. The project has received funding from the European Union's Horizon 2020 research and innovation programme under grant agreement No 634890. The authors acknowledge financial support from the I-Core program of the Israel Science Foundation (1902/12), and the Umbrella Cooperation Programme for A.M. and E.W.

Received: October 9, 2016
Revised: November 12, 2016
Published online:

[1] a) D. Branton, D. W. Deamer, A. Marziali, H. Bayley, S. A. Benner, T. Butler, M. Di Ventra, S. Garaj, A. Hibbs, X. Huang, S. B. Jovanovich, P. S. Krstic, S. Lindsay, X. S. Ling, C. H. Mastrangelo, A. Meller, J. S. Oliver, Y. V. Pershin, J. M. Ramsey, R. Riehn, G. V. Soni, V. Tabard-Cossa, M. Wanunu, M. Wiggin, J. A. Schloss, *Nat. Biotechnol.* **2008**, *26*, 1146. b) J. J. Kasianowicz, E. Brandin, D. Branton, D. W. Deamer, *Proc. Natl. Acad. Sci. USA* **1996**, *93*, 13770. c) A. Meller, in *Advances in Chemical Physics*, John Wiley & Sons, Inc., Hoboken, NJ **2012**, p. 251. d) A. Meller, L. Nivon, E. Brandin, J. Golovchenko, D. Branton, *Proc. Natl. Acad. Sci. USA* **2000**, *97*, 1079. e) B. M. Venkatesan, R. Bashir, *Nat. Nanotechnol.* **2011**, *6*, 615.
[2] a) M. Firnkes, D. Pedone, J. Knezevic, M. Döblinger, U. Rant, *Nano Lett.* **2010**, *10*, 2162. b) J. Larkin, R. Y. Henley, M. Muthukumar, J. K. Rosenstein, M. Wanunu, *Biophys. J.* **2013**, *106*, 696. c) E. C. Yusko, J. M. Johnson, S. Majd, P. Prangkio, R. C. Rollings, J. Li, J. Yang, M. Mayer, *Nat. Nanotechnol.* **2011**, *6*, 253.
[3] H.-C. Wu, H. Bayley, *J. Am. Chem. Soc.* **2008**, *130*, 6813.
[4] D. Deamer, M. Akeson, D. Branton, *Nat. Biotechnol.* **2016**, *34*, 518.
[5] a) M. Ayub, S. W. Hardwick, B. F. Luisi, H. Bayley, *Nano Lett.* **2013**, *13*, 6144. b) G. M. Cherf, K. R. Lieberman, H. Rashid, C. E. Lam, K. Karplus, M. Akeson, *Nat. Biotechnol.* **2012**, *30*, 344. c) J. Feng, K. Liu, R. D. Bulushev, S. Khlybov, D. Dumcenco,

A. Kis, A. Radenovic, *Nat. Nanotechnol.* **2015**, *10*, 1070. d) C. Cao, Y.-L. Ying, Z.-L. Hu, D.-F. Liao, H. Tian, Y.-T. Long, *Nat. Nanotechnol.* **2016**, *11*, 713.

[6] a) A. H. Laszlo, I. M. Derrington, B. C. Ross, H. Brinkerhoff, A. Adey, I. C. Nova, J. M. Craig, K. W. Langford, J. M. Samson, R. Daza, K. Doering, J. Shendure, J. H. Gundlach, *Nat. Biotechnol.* **2014**, *32*, 829. b) E. A. Manrao, I. M. Derrington, A. H. Laszlo, K. W. Langford, M. K. Hopper, N. Gillgren, M. Pavlenok, M. Niederweis, J. H. Gundlach, *Nat. Biotechnol.* **2012**, *30*, 349.

[7] M. Wanunu, *Phys. Life Rev.* **2012**, *9*, 125.

[8] a) F. Traversi, C. Raillon, S. M. Benameur, K. Liu, S. Khlybov, M. Tosun, D. Krasnozhon, A. Kis, A. Radenovic, *Nat. Nanotechnol.* **2013**, *8*, 939. b) M. Tsutsui, M. Taniguchi, K. Yokota, T. Kawai, *Nat. Nanotechnol.* **2010**, *5*, 286.

[9] B. McNally, A. Singer, Z. Yu, Y. Sun, Z. Weng, A. Meller, *Nano Lett.* **2010**, *10*, 2237.

[10] a) T. Gilboa, A. Meller, *Analyst* **2015**, *140*, 4733. b) B. N. Anderson, O. N. Assad, T. Gilboa, A. H. Squires, D. Bar, A. Meller, *ACS Nano* **2014**, *8*, 11836. c) A. Ivankin, R. Y. Henley, J. Larkin, S. Carson, M. L. Toscano, M. Wanunu, *ACS Nano* **2014**, *8*, 10774.

[11] O. N. Assad, N. Di Fiori, A. H. Squires, A. Meller, *Nano Lett.* **2015**, *15*, 745.

[12] a) H. Yamazaki, S. Kimura, M. Tsukahara, K. Esashika, T. Saiki, *Appl. Phys. A* **2014**, *115*, 53. b) F. Sawafta, B. Clancy, A. T. Carlsen, M. Huber, A. R. Hall, *Nanoscale* **2014**, *6*, 6991.

[13] a) F. Nicoli, D. Verschueren, M. Klein, C. Dekker, M. P. Jonsson, *Nano Lett.* **2014**, *14*, 6917. b) Y. Li, F. Nicoli, C. Chen, L. Lagae, G. Groeseneken, T. Stakenborg, H. W. Zandbergen, C. Dekker, P. van Dorpe, M. P. Jonsson, *Nano Lett.* **2015**, *15*, 776. c) C. R. Crick, P. Albella, B. Ng, A. P. Ivanov, T. Roschuk, M. P. Cecchini, F. Bresme, S. A. Maier, J. B. Edel, *Nano Lett.* **2015**, *15*, 553.

[14] M. Belkin, S.-H. Chao, M. P. Jonsson, C. Dekker, A. Aksimentiev, *ACS Nano* **2015**, *9*, 10598.

[15] S. Kerman, C. Chen, Y. Li, W. van Roy, L. Lagae, P. van Dorpe, *Nanoscale* **2015**, *7*, 18612.

[16] a) M. J. Levene, J. Korlach, S. W. Turner, M. Foquet, H. G. Craighead, W. W. Webb, *Science* **2003**, *299*, 682. b) J. Eid, A. Fehr, J. Gray, K. Luong, J. Lyle, G. Otto, P. Peluso, D. Rank, P. Baybayan, B. Bettman, A. Bibillo, K. Bjornson, B. Chaudhuri, F. Christians, R. Cicero, S. Clark, R. Dalal, A. deWinter, J. Dixon, M. Foquet, A. Gaertner, P. Hardenbol, C. Heiner, K. Hester, D. Holden, G. Kearns, X. Kong, R. Kuse, Y. Lacroix, S. Lin, P. Lundquist, C. Ma, P. Marks, M. Maxham, D. Murphy, I. Park, T. Pham, M. Phillips, J. Roy, R. Sebra, G. Shen, J. Sorenson, A. Tomaney, K. Travers, M. Trulson, J. Vieceli, J. Wegener, D. Wu, A. Yang, D. Zaccarin, P. Zhao, F. Zhong, J. Korlach, S. Turner, *Science* **2009**, *323*, 133.

[17] J. Larkin, M. Foquet, S. W. Turner, J. Korlach, M. Wanunu, *Nano Lett.* **2014**, *14*, 6023.

[18] D. Gérard, J. Wenger, N. Bonod, E. Popov, H. Rigneault, F. Mahdavi, S. Blair, J. Dintinger, T. W. Ebbesen, *Phys. Rev. B* **2008**, *77*, 045413.

[19] J. Wenger, D. Gérard, J. Dintinger, O. Mahboub, N. Bonod, E. Popov, T. W. Ebbesen, H. Rigneault, *Opt. Express* **2008**, *16*, 3008.

[20] M. Foquet, K. T. Samiee, X. Kong, B. P. Chauduri, P. M. Lundquist, S. W. Turner, J. Freudenthal, D. B. Roitman, *J. Appl. Phys.* **2008**, *103*, 034301.

[21] a) A. Grunwald, M. Dahan, A. Giesbertz, A. Nilsson, L. K. Nyberg, E. Weinhold, T. Ambjörnsson, F. Westerlund, Y. Ebenstein, *Nucleic Acids Res.* **2015**, *43*, 117. b) C. Dalhoff, G. Lukinavicius, S. Klimasauskas, E. Weinhold, *Nat. Chem Biol.* **2006**, *2*, 31.

[22] Y. He, M. Tsutsui, R. H. Scheicher, C. Fan, M. Taniguchi, T. Kawai, *Biophys. J.* **2013**, *105*, 776.

[23] M. Wanunu, W. Morrison, Y. Rabin, A. Y. Grosberg, A. Meller, *Nat. Nanotechnol.* **2010**, *5*, 160.

[24] A. Kinkhabwala, Z. Yu, S. Fan, Y. Avlasevich, K. Mullen, W. E. Moerner, *Nat. Photonics* **2009**, *3*, 654.

[25] M. P. Jonsson, C. Dekker, *Nano Lett.* **2013**, *13*, 1029.